JOURNAL OF MATERIALS SCIENCE 19 (1984) 1428–1438

Dislocation motion in MgO crystals under plate impact

K. S. KIM
Department of Theoretical and Applied Mechanics, University of Illinois, Urbana-Champaign, Illinois, USA

R. J. CLIFTON
Division of Engineering, Brown University, Providence, Rhode Island, USA

Dislocation dynamics in MgO single crystals is studied by means of plate impact experiments in which specimens are subjected to stress pulses of 214 to 376 MPa resolved shear stress with duration in the range of 0.09 to 0.23 μsec. Dislocation structures in the recovered crystals are observed by an etch pit technique and by transmission electron microscopy. Etch pit studies show that inclusions play a role in the generation of interior glide bands and that there is a 20 to 40-fold increase in dislocation densities outside the glide bands. Assuming the average dislocation velocity is approximately proportional to the applied stress the drag coefficient for MgO at dislocation velocities of 1 to 2 km sec^{-1} is observed to be 5×10^{-5} Nsec m^{-2}. Transmission electron microscopy determines the spacing and curvature of dislocations in glide bands.

1. Introduction

Many theoretical and experimental investigations have been carried out with the objective of understanding the relationship between microscopic dislocation dynamics and the macroscopic response of impact-loaded crystalline solids. To avoid the effects of grain boundaries and of statistical distributions of grain orientations, single crystals have been used increasingly in such investigations. Studies of the dynamics of dislocations in single crystals have included considerable work on the mobility, multiplication and nucleation of dislocations.

The mobilities of dislocations in a wide variety of materials have been reported and they are summarized in Fig. 1 for LiF [1, 2, 30], MgO [3, 4], NaCl [5, 6], GaSb [7], nickel [8], molybdenum [9], copper [10], zinc [11], niobium [12], germanium [13], silicon [14], tungsten [15], silicon–iron [16], Pb and Pb–In alloys [17], and Cu–Ni alloys [18]. Besides the study of dislocation mobility, several mechanisms [19–22] have been proposed for the multiplication of dislocations, since macroscopic plastic strain rate depends not only on the mobility of dislocations, but also on the mobile dislocation density. Also theoretical studies on the possibility of dynamic nucleation of dislocations have been made [23–27] in parallel with those investigations. However, most of the experimental work mentioned above have been at relatively low dislocation velocities (say, less than 0.01 km sec^{-1}).

Recently, Kumar and Clifton [28] have developed a plate impact experiment, for the study of dislocation motion at high velocities, that minimizes reflected waves so that the single crystal specimen can be recovered after it has been loaded by a single stress pulse. This technique was first used to obtain data on dislocation mobility in annealed, high purity LiF crystals at dislocation velocities of 0.35 to 0.85 km sec^{-1}. More recently, Vortman and Duvall [29] incorporated some of the geometrical scattering features of Kumar and Clifton's experiment [28] in the plate impact experiment of Flinn and Tinder [30] and investigated the dislocation nucleation hypothesis for shocked lithium fluoride in which Mg^{2+} ion is doped. These experiments showed that the plate

0022–2461/84 $03.00 + .12

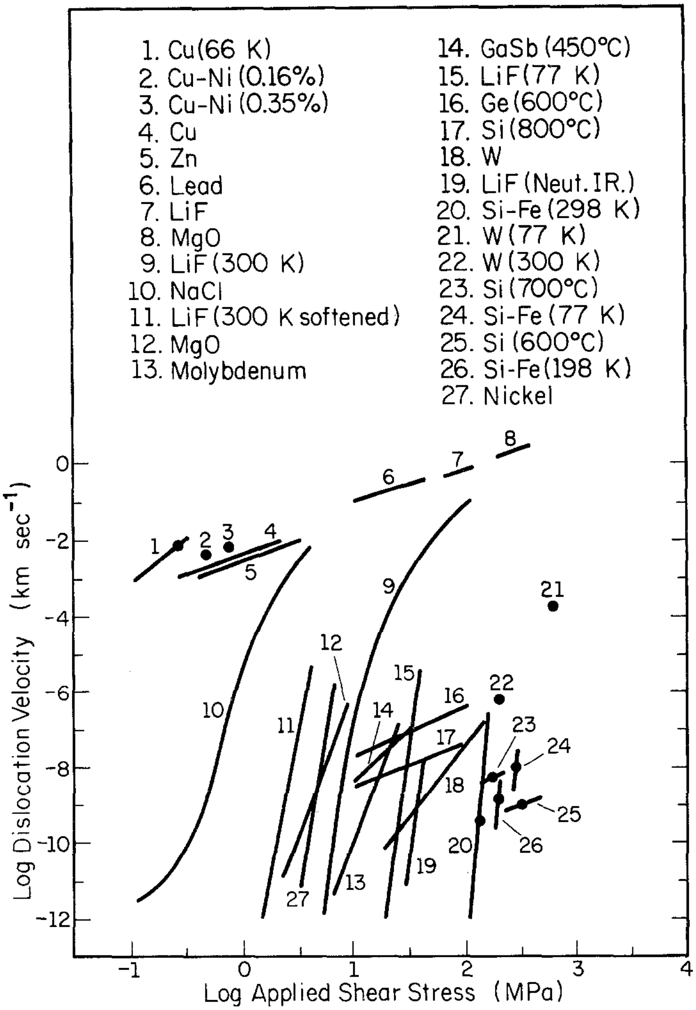

Figure 1 Dislocation mobility in various materials.

impact technique is an effective means of studying the motion of high speed dislocations.

In this work, plate impact in $\langle 1\,0\,0\rangle$ direction is used to produce square pulses of 214 to 376 MPa resolved shear strees on $\{1\,1\,0\}$ slip plane with $\langle 1\,\bar{1}\,0\rangle$ Burgers vector, with durations of 0.09 to 0.23 μsec in MgO single crystals. Dislocation configurations in the recovered crystals have been observed with an etch pit technique and with a transmission electron microscopy (TEM) has been used specifically for the observation of detailed structures of dislocations in glide bands. Different heat treatments are observed to affect the formation of interior glide bands, presumably due to the effect heat treatment has on the size of impurity clusters that can serve as sites for heterogeneous nucleation of dislocations.

2. Experimental procedure

The objective of plate impact recovery experiments on single crystal specimens is to examine changes in dislocation structures due to subjecting the specimen to a single, short duration stress pulse of known profile and recovering the specimen without further loading that would move dislocations. The short duration stress pulse is generated by impacting a target specimen with a thin flyer plate as shown in Fig. 2. The flyer plate is mounted on a foam spacer at the front of a projectile that is accelerated by a 63.5 mm diameter gas gun. The flyer is made of titanium in the shape of an octagonal star as shown in Fig. 2. Titanium is used for the flyer because its acoustic impedance (27.3×10^6 Nsec m^{-3}) is slightly lower than that of the magnesium oxide specimen (32.1×10^6 Nsec m^{-3}). As a result, the flyer separates from the specimen after the head of the pulse makes a round trip in the flyer. The octagonal star shape of the flyer, introduced by Kumar and Clifton [28], is used to minimize the effects, in a central

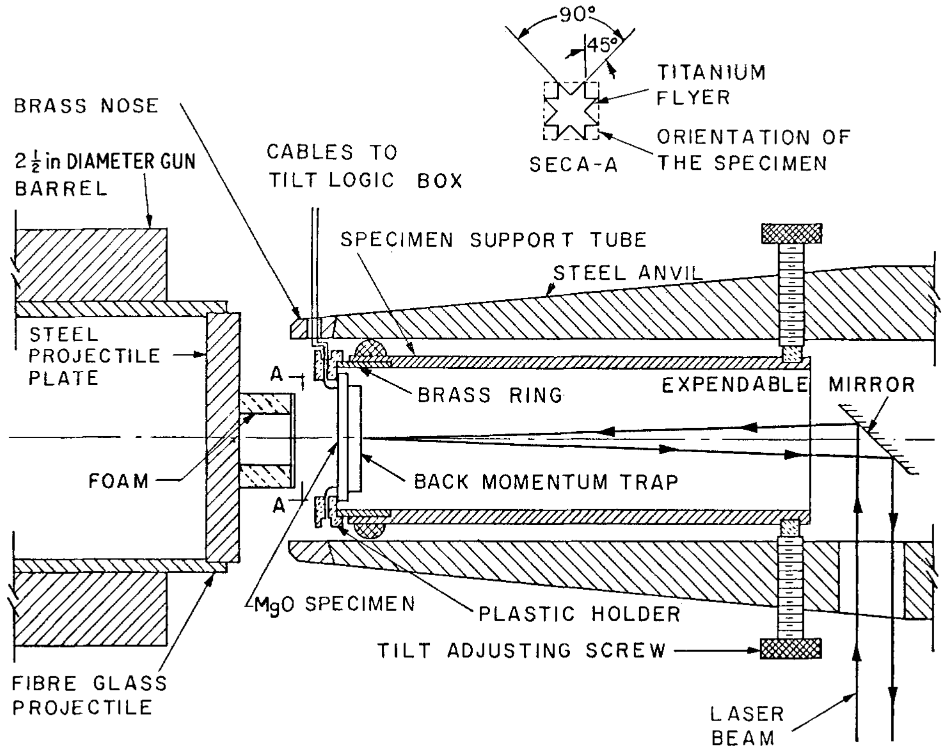

Figure 2 Schematic drawing of the plate impact experiment.

region of the specimen, of waves resulting from the finite lateral extent of the flyer and the crystal. Details of the use of star flyer have been reported by Kumar and Clifton [28].

MgO single crystal specimens were obtained from W. & C. Spicer, Ltd, UK. Each specimen has the shape of a plate cleaved on $\{1\,0\,0\}$ faces with dimensions of approximately 3 mm × 22 mm × 22 mm. The dislocation density of the crystals is 10^4 to $10^5\,\text{cm}^{-2}$ based on etch pit counts. Spectroscopic analysis shows that these crystals have a purity of 99.99%. Recorded impurities include: aluminium 1 ppm, calcium 3 ppm, chromium 1 ppm, copper $<$ 1 ppm, iron 70 ppm, nickel 3 ppm, silicon 5 ppm, and sodium $<$ 1 ppm. These high-purity crystals contain regions that are cloudy to the naked eye. This microscopic light scattering is believed to be caused by the presence of small voids, which are reported to contain hydrogen gas at 100 to 1000 bar, that was captured during crystal growth [31].

Both faces of the specimen are lapped on a 12 in. lapping machine with a cast iron lapping plate using 3 to 5 μm alumina powder and mineral oil. The specimen faces are polished further on a Texmet cloth sheet using a 3 μm diamond paste. The flatness of the polished crystal, as determined by comparison with an optical flat glass plate, is better than one band of sodium light per centimetre.

Lapping and polishing of specimens is followed by annealing heat treatments. The heat treatments are based on the studies of Stokes [32] and Miles [33] on the behaviour of dislocations and impurities under various thermal histories. The heat treatments are summarized in Table I. Specimens are annealed at 1300° C for more than 50 h in air in order to minimize the surface dislocation density generated during the surface treatments. Most of the impurities are dissolved to form a solid solution under these conditions [34, 35]. The heated specimens are cooled at various cooling rates in order to control the size of the impurities reprecipitated. Although rapid cooling (shot 78-05) should prevent clustering the impurity atoms and result in a realtively homogeneous specimen, it has the disadvantage that thermal cleavage cracks are caused by the high temperature gradients. Slow cooling (oven cooling) causes reprecipitation of the impurities. Precipitated impurities appear to act as stress concentrators and enhance the formation of glide bands.

After heat treatment, the specimens are polished further chemically in boiling orthophosphoric acid

TABLE I Summary of recovery plate impact experiment on MgO

Shot no.	Target thickness (mm)	Projectile velocity (mm $\sec^{-1}$)	Tilt angle (radian)	Pulse duration (μsec)	Momentum trap and thickness	Gap Material	Window material	Heat treatment and remarks
78-04	3.28	0.0452	1.0×10^{-3}	0.228	Titanium 2.29 mm	Vacuum	None	1300° C, 85 h anneal oven cooling (0.7° C $\min^{-1}$)
78-05	4.32	0.0405	1.8×10^{-3}	0.228	Titanium 2.29 mm	Vacuum	None	1300° C, 55 h anneal quick air cooling (150° C $\min^{-1}$) thermal crack
79-K1	3.35	0.0465	0.1×10^{-3}	0.228	High alumina 3.18 mm	Aluminium and epoxy	Glass	1300° C, 60 h anneal oven cooling (0.7° C $\min^{-1}$) first pulse missed
79-K2	2.98	0.0707	3.1×10^{-3}	0.086	High alumina 3.18 mm	Aluminium and epoxy	Glass	1300° C, 50 h anneal oven cooling (0.7° C $\min^{-1}$)
79-K3	3.52	0.0640	3.9×10^{-3}	0.228	High alumina 3.18 mm	Aluminium and epoxy	Glass	1300° C, 50 h anneal oven cooling (0.7° C $\min^{-1}$)

	MgO	Titanium	Glass	High alumina
Longitudinal wave speed (km $\sec^{-1}$)	8.95	6.07	5.64	11.88
Density (g cm^{-3})	3.58	4.50	2.32	3.45
Elastic modulus of MgO (Mb) [40]	$C_{11} = 2.87$	$C_{12} = 0.87$	$C_{44} = 1.51$	

to dissolve a 1 to 4 μm surface layer. Then an aluminium layer approximately 0.2 μm thick is vacuum deposited on the impact surface in the pattern, with which angular misalignment between the flyer and target at impact is determined by recording the times at which four voltage-biased tabs of the pattern are contacted by the flyer plate.

Good momentum-trap materials for MgO, which have a sufficiently high yield strength and an acoustic impedance that nearly matches that of MgO specimens are titanium, alumina, and boron carbide. In these experiments, α-titanium and 95% Al_2O_3 commercial high alumina were used as indicated in Table I. For shots 78-04 and 78-05, the titanium momentum traps were held by a thin, fragile glass frame which was pulled towards the specimen by four stretched rubber bands in order to minimize the gap between the specimen and the momentum trap. For shots 79-K1, 79-K2 and 79-K3, high alumina momentum traps were bonded, by an epoxy, to a 0.2 μm aluminium layer coating evaporated on to the back of the specimen. Also four lateral momentum traps of MgO crystal pieces were attached to the specimen in a similar manner, in order to further minimize the effects of the lateral unloading waves which could cause cleavage cracks.

The specimen and momentum trap assembly is located in a tube inside a hard maraging steel anvil that stops the projectile at impact so that only the momentum of the flyer is transmitted, through the specimen, into the back momentum trap. Alignment of the impact faces to ensure their parallelity is carried out by means of an optical alignment technique developed by Kumar and Clifton [36]. Development of an air cushion between the impact faces is minimized by evacuating the target chamber to a pressure of less than 200 μm Hg. The projectile velocity is determined by measuring the times at which a series of five voltage-biased, thin wire pins are shorted by contacting the front projectile plate. The distance between the nearest pins is approximately 6.35 mm and is measured to an accuracy of 0.005 mm with a travelling microscope. The times at which the pins make contact with the projectile plate are measured to an accuracy of 0.01 μsec.

A standard normal displacement interferometer is used to measure the displacement–time profile at the rear surface of the momentum trap. The light source used for the interferometer is an argon ion laser with a maximum output power of 1.5 W single mode, single frequency light of which the wave length is 0.5145 μm and the diameter of the beam is 1.3 mm. Intensity variation of the interferometer signal is detected by Monsanto MD-2 photo diodes. A Tektronix 7904 oscilloscope with a rise time of 1.5 nsec and a Tektronix 7704 oscilloscope with a rise time of 2 nsec are used to display the signal picked up by the photo diodes.

A glass window of thickness 6.35 mm is placed behind the momentum trap in order to reduce the frequency of the signal in the high velocity shots: 79-K1, 79-K2 and 79-K3. When the window materials are used the relationship between the particle velocity, $v(t)$, the wavelength, λ, of the light source, the signal frequency, $\nu(t)$, and the change in refraction index, n, and mass density, ρ, under shock loading is given by [37]

$$v(t) = \tfrac{1}{2}\lambda\nu(t)\left[\frac{1}{n-\rho(\Delta n/\Delta\rho)}\right] \qquad (1)$$

where Δ denotes differences between quantities evaluated in stressed regions where the particle velocity is to be measured and quantities evaluated in an unstressed region. However, the index of refraction n is assumed to vary with density ρ according to the Gladstone–Dale model [38] $\mathrm{d}\rho/\rho = \mathrm{d}n/n - 1$, so that the quantity in square brackets in Equation 1 becomes unity.

Crystals recovered from the plate impact experiment are cleaved on planes perpendicular to the impact face and passing near the centre of the crystal. A thin surface layer (~ 5 μm) of the crystal is dissolved (at a rate of 4 μm min^{-1}) in boiling H_3PO_4 to remove a layer damaged by the cleavage process. The surface of the crystal is then etched for 15 min in a solution of one part H_2SO_4, one part H_2O, and five parts saturated NH_4Cl. Etch pits are observed under metallurgical, optical microscopes with magnifications of x50, x100, and x250. For higher magnifications (x500 or x1000), the crystal is etched for only 5 min or less in order to produce small, non-overlapping pits.

Transmission electron microscopy is used to obtain improved resolution of dislocation structures and to obtain information on the three-dimensional geometry of these structures that is not available by observation of etch pits on surfaces. Specimens for TEM are prepared by thinning cleaved crystals in a chemical jet thinning apparatus developed by Kirkpatrick and Amelinckx [39]. The thinned specimen is mounted on an electron

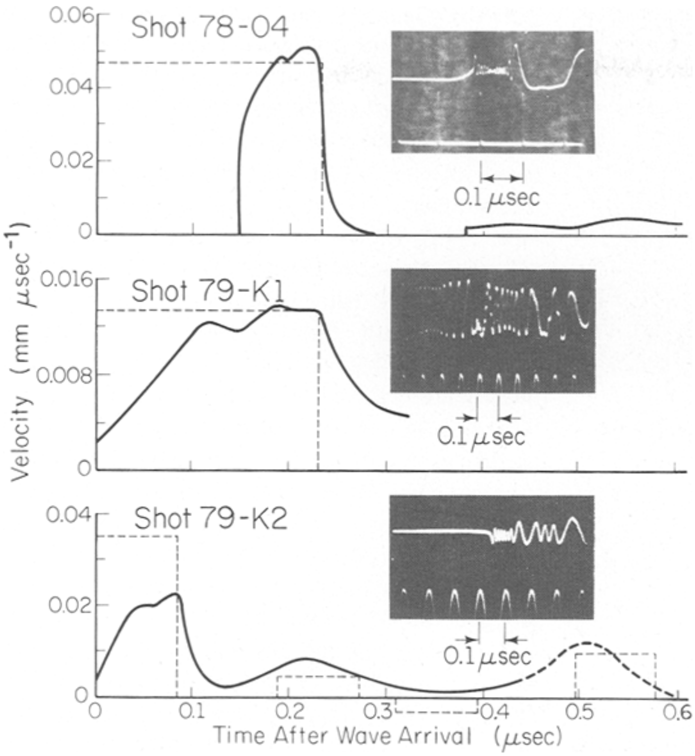

Figure 3 Velocity–time profile at the rear surface of the momentum trap (peak-to-peak intensity of the oscilogram corresponds to the displacement of $\lambda/2$, $\lambda = 0.5145\,\mu$m).

microscope specimen ring with silver paint and observed with a 100 kV transmission electron microscope.

3. Experimental results

Velocity–time profiles of the typical motions of the rear surfaces of the longitudinal momentum traps are shown in Fig. 3. Dashed lines in each figure represent the pulse predicted for purely elastic behaviour of the flyer plate, the longitudinal momentum trap and the specimen. Details of the elastic analysis including the effect of tilts between the impact faces are given in the Appendix. The front of the pulse in shot 78-04 (also 78-05) is not transmitted into the momentum trap owing to the presence of a small gap ($\sim 4\,\mu$m) between the specimen and the momentum trap. The leading part of the pulse reflects back into the specimen until the gap closes. This reflected pulse becomes a tensile pulse after it crosses the unloading wave front coming from the free back surface of the flyer plate. This tensile pulse caused micro-cleavage cracks parallel to the impact face in the specimens. The development of these cracks appears to be shown by the velocity–time profiles that follow the initial pulses in Fig. 3a. In this case, the velocity drops to zero after the initial pulse and then increases abruptly to a low level ($\sim 0.002\,$mm$\,\mu$sec^{-1}) after a quiet period of 0.1 μsec (0.03 μsec for shot 78-05). This quiet period is considered to be related to the incubation time required for crack extension at voids to begin after the tensile pulse develops. In order to avoid the micro-cracking, the remaining shots were carried out with new interface conditions which involve vacuum-evaporating a thin aluminium layer (0.2 μm) on to the back surface of the specimen and bonding the momentum trap to this layer with a thin epoxy layer ($\sim 6\,\mu$m). The interface between the aluminium layer and the specimen supports negligible tensile stress, thereby allowing the momentum trap and specimen to separate when the tensile wave arrives at the interface. The bonding between the specimen and the aluminium layer is, however, strong enough to bond the momentum trap to the specimen surface prior to impact. Even though the impedance mismatch of the layer gives a long rise time for the wave front, the crystals recovered using this technique have no microcracks due to the refelcted tensile pulse.

The velocity–time profile shown in Fig. 3b is a recording of the pulse after an additional round trip of the pulse in the momentum trap. The first arrival of the pulse was missed because of the late

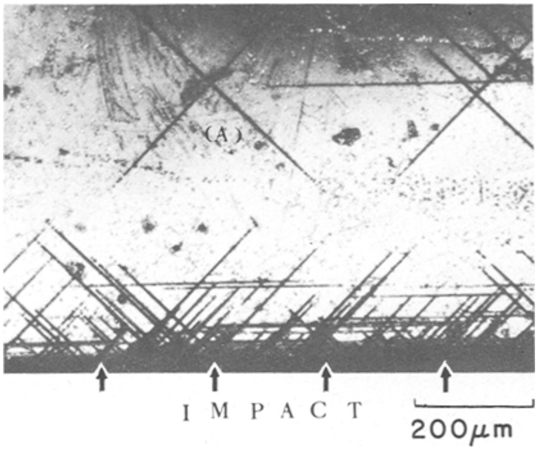

Figure 4 Etch pits on (0 1 0), perpendicular to the impact plane (shot 78-04). (1/6 of the specimen thickness near the impact face is shown. Horizontal and 45° glide bands are screw and edge dislocation bands respectively. (A) is a symmetrical internal glide band.)

triggering of the oscilloscope. The peak velocity of the pulse reaches the expected elastic value. However, the rising and falling of the front and back of the pulse are slow due to the time required for elastic waves in the aluminium–epoxy layer to "ring" up. One additional round trip of the pulse in the momentum trap increases the rise time and fall time because the pulse passes through the aluminium–epoxy layer twice more.

Fig. 3c shows the velocity–time profiles for an impact at relatively high velocities and with an unusually large tilt of the flyer at impact. In this case, although an elasticity analysis appears to be adequate for characterizing the main features of the waves in the specimen, the inclination of the wave fronts is sufficiently large for deviations of the stress state from those predicted for normal impact to be significant.

MgO is a cubic crystal with a rocksalt structure. It has six primary slip planes of $\{1\,1\,0\}$ and the slip direction of $\langle 1\,\bar{1}\,0\rangle$. However, the slip systems with slip planes perpendicular to the impact face are not activated. Under these circumstances, edge dislocation bands piercing the (0 0 1) face are expected to lead to linear etch pit arrays at 45° to the cube directions whereas screw dislocation bands piercing the (0 0 1) face are expected to lead to linear etch pit arrays parallel to the impact face. Fig. 4 shows the expected etch pits of the 45° edge dislocation bands and the 0° screw dislocation bands (shot 78-04). This figure shows about one-sixth the thickness of the crystal, including the region near the impact face, on a (0 0 1) face cleaved perpendicular to the impact face and through the centre of the crystal. Of particular interest is the appearance of so-called interior glide bands that do not intersect the original boundaries of the crystal. These interior glide bands, shown in the lower part of Fig. 4, are formed so symmetrically that intersecting bands are believed to initiate at a common inclusion. Furthermore, one-half the length of interior glide bands appears to be comparable to the length of the majority of the glide bands that intersect the surface. This result differs from that for the impact of annealed high-purity LiF crystals in which glide bands intersecting loaded surfaces were observed to be much longer than interior glide bands. The difference between these two results is believed to be due to the presence of more barriers to the motion of dislocations in the MgO used in this experiment than were present in the LiF used by Kumar and Clifton [2].

Dislocation densities outside glide bands and subgrain boundaries have been estimated in both pre-loaded and post-loaded conditions by counting the number of etch pits in a unit square of a cube face. Dislocation densities in the glide bands have been estimated by transmission electron microscopy. Initial and final dislocation densities outside of the glide bands for three shots are reported in Table II. Overall, the pulses produced a 20 to 40-fold increase in dislocation density in the

TABLE II

Shot no.	τ (MPa)	t_0 (μsec)	N_i (cm^{-2})	N_f (cm^{-2})	$\bar{d}$(μm)*	$\bar{\kappa}_{eff}$(m^{-1})†	v_d(km sec^{-1})	B(Nsec m^{-2})
78-04	232	0.228	5×10^4	0.9×10^6	280	1.03×10^{-2}	1.23	5.47×10^{-5}
79-K1	239	0.228	5×10^4	1.1×10^6	340	0.91×10^{-2}	1.46	4.65×10^{-5}
79-K2	376	0.086	5×10^4	1.9×10^6	180	2.02×10^{-2}	2.09	5.22×10^{-5}

τ, resolved shear stress; t_0, pulse duration; N_i, initial dislocation density; N_f, final dislocation density; v_d, dislocation velocity; B drag coefficient.

[*] $\bar{d}$ is the measured displacement of mobile dislocations during the pulse duration.

[†] $\bar{\kappa}_{eff}$ is the effective average curvature of dislocations at deformed state.

regions of the crystal that are remote from boundaries, while they give a 10^4 to 10^5-fold increase in the glide bands.

As a measure of the mobility of dislocations in MgO, the half-length of the longest interior glide bands is taken as indicative of the distance $\bar{d}$ that a dislocation moves during the pulse. The measured values of $\bar{d}$ and pulse duration t_0 are given in Table II. Average dislocation velocities d/t_0 as high as $2\,\mathrm{km\,sec^{-1}}$ are obtained (shot 79-K2). The values of $\bar{d}/t_0$ are used to estimate the drag coefficient B in the viscous drag model

$$\tau b = B v_d \tag{2}$$

where τ is the resolved shear traction in slip direction on the four active primary glide planes, b is Burgers vector, and v_d is the dislocation velocity. Extension of the analysis of Kumar and Clifton [2] to the case of flyers with impedance lower than that of the specimen, gives

$$\left\{\left(\frac{C_{11}-C_{12}}{2C_{11}}\right)\left[\frac{(\rho c)_f(\rho c)_s}{(\rho c)_f+(\rho c)_s}\right]V_0\right\} b = B\frac{\bar{d}}{t_0} \tag{3}$$

where $(\rho c)_f$ and $(\rho c)_s$ are longitudinal wave impedances of the flyer and of the specimen, respectively, V_0 is the initial velocity of the flyer, and t_0 is the round trip transit time of the longitudinal wave in the flyer. Experimental data required for the evaluation of B from Equation 3 are listed in Tables I and II. The value obtained for B is $5 \times 10^{-5}\,\mathrm{Nsec\,m^{-2}}$.

In order to study the change of dislocation structures, TEM is used in addition to the etch pit study. However, dislocation density in the outside glide band of the specimen is too small (order of $10^6\,\mathrm{cm^{-2}}$) for TEM. Thus, surface glide bands and interior glide bands were observed with TEM. Glide bands have a dislocation density of the order of 10^9 to $10^{10}\,\mathrm{cm^{-2}}$. A typical TEM picture of a surface glide band is shown in Fig. 5. The normal vector g of the plane used for the reflection of the electron beam is $(0\,2\,2)$ and the thickness direction of the specimen is $[1\,0\,0]$. The spacing between dislocations is approximately 0.2 to 0.3 μm. Average curvatures, $\bar{\kappa}_{\mathrm{eff}}$, of the dislocations in glide bands are given in the last column of Table II. Observations were made also with $g = (0\,0\,2)$ in order to distinguish the image of dislocations on different slip systems.

Relatively large jogs ($\sim 50\,\mathrm{nm}$) on screw dislocations, are often observed in the surface glide bands as shown in Fig. 5. A limited number of TEM observations on an interior glide band indicate that the dislocations in an interior band are more unstable under the electron beam irradiation. Spacings of dislocations in interior glide bands are also of the order of 0.3 μm. Comparison between etch pit counts and dislocation spacing observed in transmission electron microscopy show that, in many cases, single etch pits correspond to two or three dislocations in the glide bands.

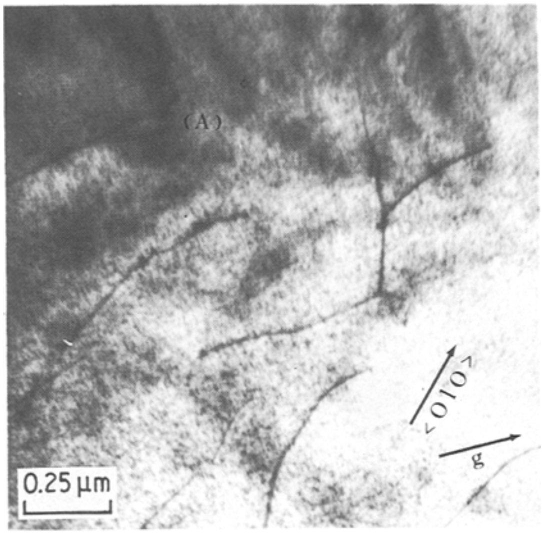

Figure 5 Transmission electron micrograph of surface glide bands. (A) is a large jog on a screw dislocation.

4. Concluding remarks

Dislocation mobility in MgO single crystals has been investigated at dislocation velocities up to $2\,\mathrm{km\,sec^{-1}}$. It appears that dislocation velocity is approximately proportional to the resolved shear stress for dislocation velocities in the range considered, i.e. 1.2 to $2.1\,\mathrm{km\,sec^{-1}}$. Furthermore, the drag coefficient B corresponding to the proportionality constant is approximately 5×10^{-5} $\mathrm{Nsec\,m^{-2}}$, which is comparable to the value obtained for viscous glide in many crystals at room temperature (see Fig. 1). Thus, it appears that the mechanism controlling mobility of dislocations in high purity crystals at room temperature is the same for many different crystals and for wide ranges of dislocation velocity.

Besides the new results on dislocation mobility at high stress levels, this investigation provides some insight into the formation of glide bands and their structures. TEM studies of the spacings, curvatures, and cusps of dislocations in glide bands appear to be promising for revealing glide band structures. Systematic variation of pulse durations combined with TEM studies are expected to be helpful in gaining further understanding of glide band formation.

Acknowledgements

This research was supported by the National Science Foundation, including support provided through the Brown University Materials Research Laboratory. This paper is based on Chapter 4 of a thesis submitted by KSK in partial fulfillment of the requirements for a PhD degree from Brown University, October 1979. The analysis reported in the Appendix was completed during KSK's summer visit at Brown University, 1982.

Appendix: Effect of tilt on wave profiles

In plate impact experiments, the alignment of the impact surfaces of the flyer and the specimen is very important. Since the velocity of the projectile is considerably less than those of waves in solids, a small tilt gives relatively large deviations of the directions of wave fronts from the normals to the impact surfaces. Consequently, the measured profile of the particle velocity at the back surface of the specimen may be distorted badly due to tilt.

A schematic diagram of an impact with tilt is shown in Fig. A1. The flyer impacts the specimen with velocity V_0 and a tilt angle ϕ. The leading edge of the contact region sweeps across the specimen in the direction N at supersonic speed. The angle between N and the x_3 axis is denoted by α. ϕ and α are measured by means of voltage biased aluminium tabs [2] coated on the front surface of the specimen. A wave with speed c propagates in the direction θ determined by

$$\sin\theta = \frac{c}{V_0}\sin\phi \qquad \text{(A1)}$$

where θ is the angle between the normal of the wave front and that of the impact surface of the specimen. The normal of the wave front has components

$$\boldsymbol{n} = \begin{bmatrix} \pm\cos\theta \\ -\sin\theta\sin\alpha \\ \sin\theta\cos\alpha \end{bmatrix} \qquad \text{(A2)}$$

where + and − signs in the bracket are for wave fronts in the specimen and flyer, respectively.

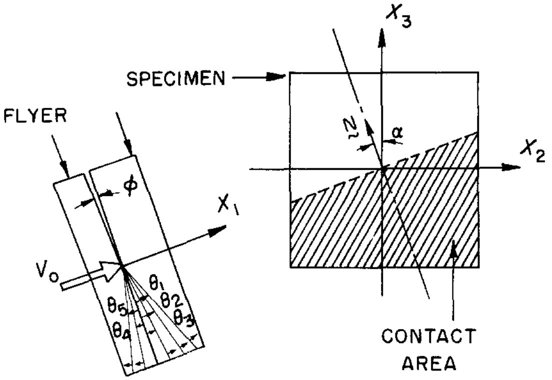

Figure A1 A diagram of wave propagation in case of tilt impact. N is direction of propagating contact boundary.

The dynamic equations for the jump $[v]$ in the particle velocity at the wave front are [42]

$$(\boldsymbol{\Gamma} - \rho c^2 \mathbf{I})\cdot[v] = 0 \qquad \text{(A3)}$$

where ρ is the mass density, $\mathbf{I}$ is the identity tensor and $\boldsymbol{\Gamma}$ is the acoustic tensor defined by

$$\boldsymbol{\Gamma} = \boldsymbol{n}\cdot\tilde{C}\cdot\boldsymbol{n} \qquad \text{(A4)}$$

in which $\tilde{C}$ is the 4th order elastic stiffness tensor of the material in which the wave propagates. The tensor $\boldsymbol{\Gamma}$ is symmetric, positive definite for materials of interest. For non-zero jumps $[v]$ the wave speed c must satisfy the characteristic equation

$$\det(\boldsymbol{\Gamma} - \rho c^2 \mathbf{I}) = 0 \qquad \text{(A5)}$$

which is a cubic equation for c^2. For $\boldsymbol{\Gamma}$ symmetric and positive definite the roots c^2 of Equation A5 are positive real numbers. For a given direction of propagation $\boldsymbol{n}$, the jump vectors $[v]$ associated with distinct wave speeds are mutaually orthogonal.

Substitution of Equations A1, A2 and A4 into Equation A5 and division by $\sin^2\theta$ gives

$$\det\left(\hat{\boldsymbol{n}}\cdot\tilde{C}\cdot\hat{\boldsymbol{n}} - \rho\frac{V_0^2}{\sin^2\phi}\mathbf{I}\right) = 0 \qquad \text{(A6)}$$

where

$$\hat{\boldsymbol{n}} = \begin{bmatrix} \pm\cot\theta \\ -\sin\alpha \\ \cos\alpha \end{bmatrix}.$$

Equation A6 is an algebraic equation of degree 6 for $\cot\theta$. From Equation A1 and the fact that there are three positive roots and three negative roots of Equation A5 it follows that Equation A6 has three roots with $\cot\theta > 0$ and three roots with $\cot\theta < 0$. The positive roots, with $\tilde{C}$ corresponding to the eleastic moduli of the target, determine the angles θ_1, θ_2, θ_3 of the wavefronts that propagate into the target. Similarly, the negative roots, with $\tilde{C}$ corresponding to the elastic moduli of the flyer, determine the angles $\theta_4, \theta_5, \theta_6$ of the wavefronts that propagate into the flyer (see Fig. A1).

For isotropic materials the acoustic tensor has the form

$$\mathbf{\Gamma} = (\lambda + \mu)\boldsymbol{nn} + \mu\mathbf{I} \tag{A7}$$

where λ is the Lamé constant, μ is the shear modulus and $\boldsymbol{nn}$ is a dyad that has $n_i n_j$ as the (i, j) component. Substitution of Equation A7 into Equatin A5 gives a characteristic equation that is independent of the angles θ, α and that has two distinct roots:

$$c_1^2 = \frac{\lambda + 2\mu}{\rho} \quad \text{for } [v] \parallel \boldsymbol{n} \tag{A8a}$$

$$c_2^2 = \frac{\mu}{\rho} \quad \text{for } [v] \perp \boldsymbol{n} \tag{A8b}$$

The root $c_2^2 = \mu/\rho$ is a repeated root. Thus, when an isotropic flyer is used the angles θ_4 and θ_5 obtained from Equations A8b and A1 are equal. This angle is denoted by θ_4 and θ_6 obtained from Equations A8a and A1 is denoted by θ_5 in Fig. A1.

Once the angles θ_1, θ_2, . . . , θ_6 are obtained from Equation A6 the jumps $[v]_i$ across the wavefronts can be obtained from Equation A3 except for scalar amplitudes A_i, $i = 1, \ldots, 6$ that are determined from boundary conditions at the impact face. Since these boundary conditions involve the surface tractions on the impact face, it is necessary to consider jumps in stresses across the wavefronts. The jump $[\boldsymbol{\sigma}]_i$ in the stress tensor $\boldsymbol{\sigma}$ across the wavefront with normal $\boldsymbol{n}_i$ is

$$[\boldsymbol{\sigma}]_i = -\frac{1}{c_i}\tilde{C}:(\boldsymbol{n}_i[v]_i) \quad i = 1, \ldots, 6 \tag{A9}$$

where c_i is the velocity of the wavefront. Summation of the discontinuities across the wavefronts in the target and the flyer give, respectively, the following expressions for the stress states at the impact face.

$$\boldsymbol{\sigma}^{(\mathrm{t})} = -\sum_{i=1}^{3} \frac{1}{|c_i|}\tilde{C}^{(\mathrm{t})}:(\boldsymbol{n}_i[v]_i) \tag{A10a}$$

$$\boldsymbol{\sigma}^{(\mathrm{f})} = -\sum_{i=4}^{6} \frac{1}{|c_i|}\tilde{C}^{(\mathrm{f})}:(\boldsymbol{n}_i[v]_i). \tag{A10b}$$

Continuity of surface tractions requires

$$\boldsymbol{e}_j \cdot \boldsymbol{\sigma}^{(\mathrm{t})} \cdot \boldsymbol{e}_1 = \boldsymbol{e}_j \cdot \boldsymbol{\sigma}^{(\mathrm{f})} \cdot \boldsymbol{e}_1 \quad j = 1, 2, 3 \tag{A11}$$

where $\boldsymbol{e}_1$ is a unit normal to the impact face. Substitution of Equation A10 into Equation A11 and use of

$$[v]_i = A_i[\hat{v}]_i \quad i = 1, \ldots, 6 \tag{A12}$$

where $[\hat{v}]_i$ are unit vectors and A_i are the amplitudes to be determined, gives three linear equations for the six unknows A_i

$$\sum_{i=1}^{3} \frac{1}{|c_i|}\boldsymbol{e}_j \cdot \{\tilde{C}^{(\mathrm{t})}: (\boldsymbol{n}_i[\hat{v}]_i)\} \cdot \boldsymbol{e}_1 A_i - \sum_{i=4}^{6} \frac{1}{|c_i|}\boldsymbol{e}_j \cdot \{\tilde{C}^{(\mathrm{f})}:(\boldsymbol{n}_i[\hat{v}_i])\} \cdot \boldsymbol{e}_1 A_i = 0 \tag{A13}$$

where $j = 1, 2, 3$.

The remaining three equations are obtained from the condition that the particle velocity be continuous across the impact face. This condition

$$\sum_{i=1}^{3} A_i[\hat{v}]_i - \sum_{i=4}^{6} A_i[\hat{v}]_i = V_0 \tag{A14}$$

where V_0 in the particle velocity of the flyer before impact. Equations A13 and A14 are the required six equations for the six unknowns A_i. Alternately, if the boundary condition at the impact face is one of zero shear traction, then Equation A14 becomes a single equation corresponding to the continuity of the normal component of particle velcoity. The remaining five equations are Equations A13 for $j = 1$ plus four equations obtaining from requiring the two sums in Equation A13 to vanish identically for $j = 2$ and $j = 3$. When an isotropic flyer is used, for eight unknowns A_i, $i = 1, \ldots, 5$, and three components of $[\hat{v}]_4$, $[\hat{v}]_4 \cdot \boldsymbol{n}_4 = 0$ and $\|[\hat{v}]_4| = 1$ together with Equations A13 and A14 with summation limits up to 5 instead of 6, provide eight independent equations.

Transmission and reflection of the multiple waves at the interface of the specimen and momentum trap are treated in a similar manner. The complete velocity–time profile at the rear surface of the momentum trap, due to elastic impact with tilt is presented in Fig. 3c. Conditions of no slip on the interfaces are assumed.

References

1. W. G. JOHNSTON and J. J. GILMAN, *J. Appl. Phys.* **30** (1959) 129.

2. P. KUMAR and R. J. CLIFTON, *ibid.* **50** (1979) 4747.
3. R. N. SINGH and R. L. COBLE, *ibid.* **45** (1974) 981.
4. *Idem, ibid.* **45** (1974) 990.
5. E. Y. GUTMANAS, E. M. NADGORNYI and A. V. STEPANOV, *Sov. Phys. Solid State* **5** (1963) 743.
6. H. STRUNK, *Mater. Sci. Eng.* **26** (1976) 231.
7. A. R. CHAUDHURI, J. R. PATEL and L. G. RUBIN, *J. Appl. Phys.* **33** (1962) 2736.
8. R. W. ROHDE and C. H. PITT, *ibid.* **38** (1967) 876.
9. H. L. PREKEL and H. CONRAD, *"Dislocation Dynamics"*, edited by A. R. Rosenfield, *et al.* (McGraw-Hill, 1968) p. 431.
10. K. M. JASSBY and T. VREELAND, Jr., *Phil. Mag.* **21** (1970) 1147.
11. D. P. POPE and T. VREELAND Jr, *ibid.* **20** (1969) 1163.
12. H. D. GUBERMAN, *Acta Metall.* **16** (1968) 713.
13. R. L. BELL and W. BONFIELD, *Phil. Mag.* **9** (1964) 9 (see also [7]).
14. P. HAASEN, *"Dislocation Dynamics"*, edited by A. R. Rosenfield *et al.* (McGraw-Hill, 1968) p. 701.
15. H. W. SCHADLER, *Acta Metall.* **12** (1964) 861.
16. D. W. MOON and T. VREELAND, Jr., *J. Appl. Phys.* **39** (1968) 1766.
17. V. R. PARAMESWARAN and J. WEERTMAN, *Met. Trans.* **2** (1971) 1233.
18. T. SUZUKI, *"Dislocation Dynamics"*, edited by A. R. Rosenfield, *et al.* (McGraw-Hill, 1968) p. 551.
19. F. C. FRANK and W. T. READ, *Phys. Rev.* **79** (1950) 722.
20. J. S. KOEHLER, *ibid.* **86** (1952) 52.
21. S. AMELINCKX and W. DEKEYSER, *J. Appl. Phys.* **29** (1958) 1000.
22. A. S. TETELMAN, *Acta Metall.* **10** (1962) 813.
23. J. WEERTMAN, "Metallurgical Effects at High Strain Rates" (Plenum, New York, 1973) p. 319.
24. C. S. SMITH, *Trans. Met. Soc. AIME* **212** (1958) 574.
25. Y. Y. EARMME and J. H. WEINER, *J. Appl. Phys.* **48** (1977) 3317.
26. J. H. WEINER and M. PEAR, *Phil. Mag.* **31** (1975) 679.
27. F. C. FRANK, "Report of the Conference on Strength of Solids" (Physical Society, London, 1948) p. 46.
28. P. KUMAR and R. J. CLIFTON, *J. Appl. Phys.* **48** (1977) 4850.
29. J. E. VORTHMAN, PhD thesis, Washington State University (1979).
30. J. E. FLINN and R. F. TINDER, *Scripta Metall.* **8** (1974) 689.
31. Y. CHEN, private communication.
32. R. J. STOKES, *J. Amer. Ceram. Soc.* **49** (1966) 39.
33. G. D. MILES, *J. Appl. Phys.* **36** (1975) 1471.
34. R. J. STOKES, *J. Amer. Ceram. Soc.* **48** (1965) 60.
35. R. N. SINGH and R. L. COBLE, *J. Appl. Phys.* **45** (1974) 5129.
36. P. KUMAR and R. J. CLIFTON, *ibid.* **48** (1977) 1366.
37. L. M. BARKER and R. E. HOLLENBACH, *ibid.* **41** (1970) 4208.
38. J. H. GLADSTONE and T. P. DALE, *Trans. Roy. Soc. (London)* **A148** (1958) 887.
39. H. B. KIRKPATRICK and S. AMELINCKX, *Rev. Sci. Instrum.* **33** (1962) 488.
40. G. SIMMONS and H. WANG, "Single Crystal Elastic Constants and Calculated Aggregate Properties" (M.I.T. Press, 1971).
41. W. E. ELKINGTON, G. THOMAS and J. WASHBURN, *J. Amer. Ceram. Soc.* **46** (1963) 307.
42. M. J. P. MUSGRAVE, *"Crystal Acoustics"* (Holden Day, San Francisco, 1970) p. 84.

Received 7 February
and accepted 18 May 1983